Coastal Engineering 120 (2017) 78–92

Contents lists available at ScienceDirect

Coastal Engineering

journal homepage: www.elsevier.com/locate/coastaleng

Observations and 3D hydrodynamics-based modeling of decadal-scale shoreline change along the Outer Banks, North Carolina

I. Safak[a,*], J.H. List[a], J.C. Warner[a], N. Kumar[b]

[a] United States Geological Survey, Coastal and Marine Geology Program, Woods Hole Coastal and Marine Science Center, 384 Woods Hole Rd, Woods Hole, MA 02543, USA

[b] Department of Civil and Environmental Engineering, University of Washington, Seattle, WA 98115, USA

ARTICLE INFO

Keywords:
Sediment transport
Shoreline change
Alongshore transport
Outer Banks
NC
Aerial photography
COAWST
ROMS
SWAN
Three-dimensional
Modeling
Wave modeling
Nearshore modeling
Model coupling

ABSTRACT

Long-term decadal-scale shoreline change is an important parameter for quantifying the stability of coastal systems. The decadal-scale coastal change is controlled by processes that occur on short time scales (such as storms) and long-term processes (such as prevailing waves). The ability to predict decadal-scale shoreline change is not well established and the fundamental physical processes controlling this change are not well understood. Here we investigate the processes that create large-scale long-term shoreline change along the Outer Banks of North Carolina, an uninterrupted 60 km stretch of coastline, using both observations and a numerical modeling approach. Shoreline positions for a 24-yr period were derived from aerial photographs of the Outer Banks. Analysis of the shoreline position data showed that, although variable, the shoreline eroded an average of 1.5 m/yr throughout this period. The modeling approach uses a three-dimensional hydrodynamics-based numerical model coupled to a spectral wave model and simulates the full 24-yr time period on a spatial grid running on a short (second scale) time-step to compute the sediment transport patterns. The observations and the model results show similar magnitudes ($O(10^5\ m^3/yr)$) and patterns of alongshore sediment fluxes. Both the observed and the modeled alongshore sediment transport rates have more rapid changes at the north of our section due to continuously curving coastline, and possible effects of alongshore variations in shelf bathymetry. The southern section with a relatively uniform orientation, on the other hand, has less rapid transport rate changes. Alongshore gradients of the modeled sediment fluxes are translated into shoreline change rates that have agreement in some locations but vary in others. Differences between observations and model results are potentially influenced by geologic framework processes not included in the model. Both the observations and the model results show higher rates of erosion (~−1 m/yr) averaged over the northern half of the section as compared to the southern half where the observed and modeled averaged net shoreline changes are smaller (< 0.1 m/yr). The model indicates accretion in some shallow embayments, whereas observations indicate erosion in these locations. Further analysis identifies that the magnitude of net alongshore sediment transport is strongly dominated by events associated with high wave energy. However, both big- and small-wave events cause shoreline change of the same order of magnitude because it is the gradients in transport, not the magnitude, that are controlling shoreline change. Results also indicate that alongshore momentum is not a simple balance between wave breaking and bottom stress, but also includes processes of horizontal vortex force, horizontal advection and pressure gradient that contribute to long-term alongshore sediment transport. As a comparison to a more simple approach, an empirical formulation for alongshore sediment transport is used. The empirical estimates capture the effect of the breaking term in the hydrodynamics-based model, however, other processes that are accounted for in the hydrodynamics-based model improve the agreement with the observed alongshore sediment transport.

1. Introduction

Coastal erosion is a major societal concern as the majority of the shorelines worldwide are estimated to be eroding [16,14,28,6,44,37,20]. Considering that most of the population growth is occurring near coasts [46], the growing demand on these locations due to tourism, recreation, and habitat conservation will continue to increase. Therefore, accurate information of shoreline change is needed for better coastal zone manage-

* Corresponding author.
E-mail addresses: isafak@usgs.gov (I. Safak), jlist@usgs.gov (J.H. List), jcwarner@usgs.gov (J.C. Warner), nirni@uw.edu (N. Kumar).

http://dx.doi.org/10.1016/j.coastaleng.2016.11.014
Received 18 December 2015; Received in revised form 15 November 2016; Accepted 22 November 2016
Available online 10 December 2016
0378-3839/ Published by Elsevier B.V.

ment. Shoreline positions can be delineated from sources such as local surveys and aerial photographs. The change of shoreline position can be computed as a change rate, but needs to be derived and presented carefully, as the positions may often be measured after major storm events and not necessarily reflect the long-term trend. The change of shoreline position due to instantaneous rates of sediment movement is not practical to measure with adequate spatial and temporal resolution. This increases the importance of numerical models which can be used to investigate the processes driving large-scale, long-term shoreline change.

Observations suggest that sediment characteristics, natural underlying geologic framework, and anthropogenic effects on bathymetry (e.g., extraction of shelf sediment for beach nourishment) may influence coastal evolution [50,55,6,42,7,35,15,56,77], however, long-term shoreline change is primarily thought to be controlled by alongshore variation of alongshore sediment transport in the surf zone, with contributions from sea level rise and dune and inlet processes. Throughout the past few decades, several empirical models of cross-shore integrated alongshore sediment transport rate have been proposed for practical use. Most of these formulations have been strongly based on depth-limited wave breaking characteristics [29,67] while simulating formation of large-scale shoreline instabilities associated with high-angle deep water waves requires the models to be based on deep water wave height and angle [18,2]. Some other approaches additionally account for variation of other parameters such as beach properties (slope and sediment size; [26]), depth-averaged currents [5] or breaker type [59]. It has been noted several times that the coefficients in such empirical formulations of alongshore sediment transport are extremely poorly constrained and span a few orders of magnitude [29,71,61,16,51,59], which indicates not only site-dependency but also possible problems with the formulations themselves and their calibration with observations (e.g., sand tracers; [29]; streamer sediment traps; [71]). Using such empirical formulations, long-term shoreline change has been modeled using one-line diffusion models (e.g., [19]), which are very computationally efficient and require a minimal set of inputs, and also n-line models (e.g., [12]) which model multiple contour lines but can exhibit instabilities [49]. These models are typically based on simplifications on bathymetry that may ignore processes relevant to a given site (e.g., presence of offshore topography), and their assumptions related to wave propagation (shoaling, refraction, breaking) may preclude capturing the complex processes important in most nearshore environments [27].

The listed limitations of empirical formulations overall increase the importance of hydrodynamics-based approaches in alongshore sediment transport modeling. In spite of having limitations such as numerical coding complications and computational expense, hydrodynamics-based models account for more complete physics, allow higher spatial resolution and, therefore, more in-depth diagnosis of processes. The simplest hydrodynamics-based approach to model alongshore sediment transport is using a one-dimensional (1-D) cross-shore profile model (e.g., [52,70]). These models either take as input or compute cross-shore distribution of waves to model depth-averaged currents by assuming that transport at each profile can be calculated independent of the others, i.e., they do not account for terms in the momentum balance such as alongshore advective accelerations or pressure gradients. Their errors in computations of alongshore currents in three-dimensional (3-D) field conditions were noted to be high, therefore, the ideal conditions to test these type of models can be achieved using wave flumes in laboratory experiments [69].

Depth-averaged two-dimensional (2-D) models (sometimes referred as ‘coastal area’ models) also return depth-averaged alongshore currents and sediment fluxes but include the effect of advective accelerations and pressure gradients (e.g., [78]). The lack of accounting for these momentum terms can account for the discrepancy between transport estimates found using the empirical approaches versus more sophisticated hydrodynamics-based models [38,39]. Kaergaard and Fredsoe [25] recently used a depth-averaged 2-D hydrodynamics-based model to estimate wave-induced alongshore sediment transport and coupled that model to a one-line model. Their morphodynamic model showed formation and evolution of cuspate coasts, spits and undulations on centennial scales depending on wave energy and directionality and shoreline curvature.

Fully 3-D models simulate currents and sediment transport on three-dimensional grids. In addition to the cross-shore variability of alongshore sediment transport [69,32] and alongshore advective processes [25], these models can also resolve the vertical structure of the flow and the bottom boundary layer processes which could be essential for better modeling of sediment transport patterns in response to the flow field and bathymetric features [13]. Therefore, coupling of 3-D hydrodynamics-based models with wave and sediment transport algorithms provides a better representation of the underlying physics along with capability to include relevant processes and interactions occurring at different temporal and spatial scales, albeit at a higher computational cost. So far, to the authors' knowledge, a 3-D hydrodynamics-based model has not been used for investigating large-scale long-term sediment transport patterns, likely due to the computational expense of such models. With recent and continuing increase in computing power, the use of these 3-D hydrodynamics-based models has become a viable approach for investigating long-term large-scale sediment processes in the nearshore. This approach and the underlying assumptions in such an analysis still need to be evaluated in detail with comprehensive, high-resolution observations and realistic bathymetry, atmospheric, wave, and current forcing for the models. The main objective of this study is to investigate the processes that create large-scale long-term shoreline change. Following an introduction of the study site (Section 2), a dense data set of shorelines covering almost three decades is analyzed and long-term shoreline change is quantified (Section 3). That section also introduces the data sets (bathymetry, atmospheric, hydrodynamic, and wave data) used for model setup and testing. Then, a coupled 3-D hydrodynamic and sediment transport model (simulated using a morphostatic sense) and a phase-averaged wave model are used for investigating the physical processes that create this change (Section 4). The modeling system is used on decadal time scales and spatial scales of tens of km. The comparison between observed and modeled shoreline change reveals the degree to which the advanced modeling approach incorporates the processes relevant to long-term change, and the ability to provide an increased understanding of the fundamental processes driving this change (Section 5). Although it is beyond the scope of this effort to compare results to all the previous empirical and process-based approaches, the advanced hydrodynamics-based model is then compared to a simple but the most-commonly used empirical formulation to assess the significance of using a more detailed approach. Further discussions are made in Section 6 and the conclusions are summarized in Section 7.

2. Study site: Outer Banks of North Carolina

We investigate shoreline change along the Outer Banks of North Carolina of the US East Coast (Fig. 1) for a 65-km section of coastline between Oregon Inlet in the north and Cape Hatteras in the south. This section of the barrier island acts as a buffer for Pamlico and Albemarle Sounds against the Atlantic Ocean (Fig. 1). The current rate of relative sea-level rise in the area is about 4 mm/yr and is among the highest along the Atlantic Coast of the United States [54]. There is no direct river input and the coast is fairly continuous with no major human intervention (except dune maintenance) such as coastal structures, to interrupt alongshore processes [37]. This region of the coastline is impacted by frequent high-energy storm events (e.g., [50,53]) and offers a prime environment to investigate long-term sediment transport due to atmospheric and hydrodynamic conditions.

On a decadal time-scale, the shoreline along the Outer Banks is recessing ~O(1 m/yr), with relatively high erosion rates at Cape Hatteras and Oregon Inlet (~5 m/yr in the latter; [24]). The wave

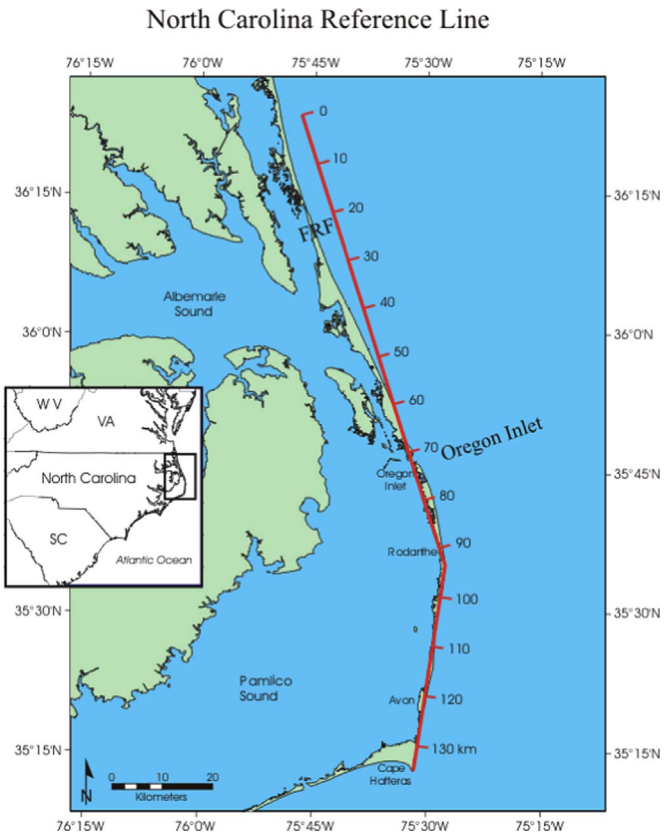

Fig. 1. Map of the Outer Banks, the barrier island chain at the North Carolina coast. The alongshore distance scale is used in subsequent Figs. 2, 8, 9, 11 and 12; the focus of this study is between 70–135 km.(For interpretation of the references to color in this figure legend, the reader is referred to the web version of this article.)

climate is characterized as low-angle and the Outer Banks is described as a diffusive shoreline, based on wave data from buoys off Field Research Facility at Duck, NC and Wave Information Study (WIS) hindcasts [3]. Similarly, the analysis of Lazarus and Murray [34] showed that the northern North Carolina coast is low-angle-wave dominated and promontories (which can be informally referred as 'bumps') erode and embayments accrete, i.e., morphological features along the shoreline have diffused.

3. Observations

3.1. Shoreline data

In this study, shoreline position data were derived from 14 sets of georeferenced aerial photographs of the coast between Oregon Inlet and Cape Hatteras [21]. The photographs were taken between December 1978 – October 2002, corresponding to mostly late summer and early fall. The interpreted 'High Water Line' shorelines (proxy based on the wet/dry line) were obtained by digitizing the georeferenced aerial photographs. Using the time series of 14 shoreline position at each location along the coast, the rate of shoreline change was computed as the slope of a standard linear regression. Tests demonstrate that exclusion of the three shorelines that were not collected in late summer/early fall made very little difference in the results. The 95% confidence interval (CI) on the linear regression slope serves as a measure of the shoreline change rate significance – if the calculated rate plus or minus the CI encompasses a zero change rate, the rate is not considered significant. The reader is referred to Hapke and Henderson [21] for further details such as quality control on the data set, how tide effects are taken into account in processing, etc.

3.2. Bathymetric data

The topographic and bathymetric data used for generating the model grid elevation surfaces are acquired from several different sources. Topographic/bathymetric LIght Detection And Ranging (LIDAR) data set was collected in August 2009 and covers land and shallow areas along the section of interest, extending inland 500 m and offshore to laser extinction (http://coast.noaa.gov/dataviewer/webfiles/metadata/usace2009_nc_template.html?redirect=301ocm). In addition to this, US Geological Survey collected single-beam and swath bathymetric data that covers the inner continental shelf (collected in 2001 and 2002; [62]). These sources were combined with the NOAA Coastal Relief Model and ETOPO-2 bathymetry to create a merged continuous surface of elevation data.

3.3. Atmospheric, hydrodynamic, and wave data

Lateral boundary conditions for surface waves were prescribed using the 31-yr WaveWatchIII hindcast (1979–2009; [11]) of National Centers for Environmental Prediction (NCEP). In the boundary conditions, waves were parametrized with a JONSWAP spectrum using the 3-hourly average hindcasts of significant wave height, spectral peak period and peak direction. For momentum flux at the ocean surface, wind-induced stress was calculated using the 3-hourly averaged wind fields at 10-m above the sea surface, based on the 32-km resolution hindcasts of North American Regional Reanalysis (NARR; ftp://ftp.cdc.noaa.gov/Datasets/NARR/monolevel/) of NOAA. Tidal forcing was imposed using constituents derived from the US Atlantic Coast ADCIRC database [45]. In addition to these hindcasts of waves, winds, and tides that were used as model forcings, field observations of waves from nearby buoys available (1996–2002) and a nearshore experiment in 2010 within the section of interest [40,31] were used for validation of the model.

4. Hydrodynamics-based modeling

4.1. Hydrodynamics

The hydrodynamic, wave, and sediment transport processes are modeled with the hydrodynamics-based, three-dimensional, Coupled Ocean-Atmosphere-Wave-Sediment Transport modeling system (COAWST). COAWST is an open-source modeling system developed to simulate atmospheric processes, oceanographic circulation, surface waves and tracer transport of salinity, temperature, sediment and biological quantities in the coastal ocean, estuaries and bays [73,75]. The oceanographic component in COAWST is the Regional Ocean Circulation Model (ROMS; [57]), which has been widely accepted and tested in many ocean scale, coastal and estuarine applications. ROMS solves the three-dimensional primitive Reynolds-averaged momentum equations with horizontal and vertical advection, Coriolis acceleration terms, and wave effects on currents [30]. The vertical turbulent mixing is parametrized with the two-equation Generic Length Scale (GLS) turbulence closure model [66] implemented with the option of accounting for wave-breaking-induced surface fluxes of Turbulent Kinetic Energy [72]. The model resolves wetting and drying processes at grid cells by preventing outward water flux from dry cells with depths less than a user-specified value [76]. The modeling system used full three-dimensional formulations here. We show below the simplified depth-averaged form of the alongshore momentum balance (which is investigated in detail in Section 5.4):

$$D\frac{\partial \overline{v}}{\partial t} + D\left[\frac{\partial(\overline{u}\overline{v})}{\partial x} + \frac{\partial(\overline{v}\overline{v})}{\partial y} + \overline{v}\frac{\partial \overline{u^{st}}}{\partial x} + \overline{v}\frac{\partial \overline{v^{st}}}{\partial y}\right] + Df(\overline{u} + \overline{u^{st}})$$
$$= D\,\overline{F^{wy}} - D\frac{\partial \overline{\phi}}{\partial y} - D\overline{u^{st}}\left(\frac{\partial \overline{v}}{\partial x} - \frac{\partial \overline{u}}{\partial y}\right) + \frac{\tau_{sy}}{\rho} - \frac{\tau_{by}}{\rho}, \quad (1)$$

where D is total water depth, t is time, x is the cross-shore distance, y is the alongshore distance, $\overline{u}$ and $\overline{v}$ are the vertically-integrated Eulerian mean velocities in the cross-shore and alongshore directions, respectively, $\overline{u^{st}}$ and $\overline{v^{st}}$ are the vertically-integrated Stokes velocities in the cross-shore and alongshore directions, respectively, f is the Coriolis parameter, ϕ is the geopotential function, F^{ω} is the momentum flux from non-conservative wave terms, τ_s is the surface stress, τ_b is the bottom stress, and ρ is the water density. The first term on the left hand side is local acceleration, followed by the horizontal advection and the Coriolis force. The terms on the right hand side are the alongshore components of the non-conservative wave forcing (wave breaking), pressure gradient, horizontal vortex force (described below), surface stress and bottom stress, respectively.

4.2. Surface waves

COAWST uses the Model-Coupling-Toolkit [33,74,75] to fully couple ROMS with a spectral surface gravity wave propagation model, Simulating WAves Nearshore (SWAN; [9]). SWAN computes the spectral evolution of waves by solving the wave action balance equation in two horizontal Cartesian coordinates and wave direction domain:

$$\frac{\partial N}{\partial t} + \frac{\partial c_x N}{\partial x} + \frac{\partial c_y N}{\partial y} + \frac{\partial c_\sigma N}{\partial \sigma} + \frac{\partial c_\theta N}{\partial \theta} = \frac{S}{\sigma}, \tag{2}$$

where N is the wave action density (energy density divided by relative frequency), c is wave propagation velocity, σ is the relative wave frequency, θ is the wave direction, and S is the sum of source and sink terms into the wave field, i.e., wind input, breaking, bottom friction and nonlinear wave-wave interactions. Two-way ROMS-SWAN model coupling occurs within user-defined coupling intervals: changing water levels and current velocities from ROMS modify wavelength and therefore wave propagation; in turn, wave height, period, direction and dissipation rate from SWAN are used for calculating wave-induced effects on mean currents. It has been documented that influence of wave-induced flows and mixing in ocean circulation are essential, especially in surf zone processes in the nearshore (e.g., [30]). Wave-induced effects on mean currents are accounted for in the integration of the momentum equations of COAWST; momentum contribution of waves on mean flow due to the interaction between the Stokes drift (non-Eulerian mean flow due to waves) and the mean flow vorticity is modeled with the Vortex Force formalism method [58,64,65]. This method allows the decomposition of the conservative (advective flows) and non-conservative (breaking-induced flows) contributions of surface waves on the momentum balance. The conservative contributions are relatively more important outside the surf zone on the inner shelf, and the non-conservative contributions are important only within the surf zone. This approach has been used to successfully simulate nearshore flow settings by Olabarrieta et al. [47] and applications to other surf zone processes in Kumar et al. [30]. Wave-current interaction at the bottom boundary layer, which enhances bottom shear stress due to turbulence within the relatively thin wave boundary layer (e.g., [41]) and therefore influences sediment transport, is parameterized with the formulation presented by Warner et al. [73].

4.3. Sediment transport

Sediment transport is computed using suspended sediment and bedload transport algorithms [73]. The scalar transport equation for suspended sediment is:

$$\frac{\partial (H_z C)}{\partial t} + \frac{\partial (u H_z C)}{\partial x} + \frac{\partial (v H_z C)}{\partial y} + \frac{\partial (\Omega H_z C)}{\partial s} = -\frac{\partial}{\partial s}\left(\overline{C'w'} - \frac{\nu_\theta}{H_z}\frac{\partial C}{\partial s}\right) + C_{source}, \tag{3}$$

where H_z is the grid-cell thickness, z is the vertical coordinate, C is the suspended sediment concentration, u, v, and Ω are the components of Lagrangian flow velocity in the horizontal (x and y) and vertical sigma (s) coordinates, a prime ($'$) indicates a fluctuating turbulent quantity, w' is the turbulent velocity in s-direction, ν_θ is the kinematic molecular diffusivity, and C_{source} is a sediment source/sink term which represents the exchange with the bed, i.e., net exchange of vertical settling and upward flux of sediment eroding from the bed. Bedload transport rate is calculated as follows:

$$q_{bl} = \Phi\sqrt{(m-1)gD_{50}^3}\,\rho_s, \tag{4}$$

in kg/m/s where Φ is the non-dimensional transport rate defined for the case of combined effects of mean currents and asymmetrical waves (for details, see [60]), m is the specific gravity of the primary sediment particle, g is the gravitational acceleration, D_{50} is the median diameter of the primary sediment particle, and ρ_s is the density of the primary sediment particle. Total sediment volume transport is obtained as the summation of this bedload component and the vertically integrated suspended sediment flux component. Some sediment transport processes are not accounted for in the modeling simulations, such as aeolian transport and overwash. Wind-blown sand is locally transported into dunes, however, no large-scale alongshore transport is expected. For overwash, no historically major events occurred during the study period of interest (1979–2002); it is also known that in case of overwash events, the overwashed sand along the section of interest is typically returned to the dune line by heavy equipment. It should also be noted that groins are not implemented in the model, although a set of short groins for the protection of the Cape Hatteras Lighthouse (since moved) exist at about 131-km (Fig. 2) and appear to affect the shape of the shoreline only in that immediate vicinity.

The model computations of sediment transport are converted to shoreline change by computing the alongshore gradients of the cross-shore integrated alongshore sediment fluxes. Accordingly, the shoreline change rate is calculated as:

$$\frac{\partial x}{\partial t} = -\frac{1}{d}\frac{\partial Q}{\partial y}, \tag{5}$$

where d is the closure depth (maximum water depth for which the cross-shore profile is assumed to shift in response to erosion and accretion), and Q is the net, cross-shore integrated alongshore sediment transport flux. Sensitivity tests on the cross-shore range of integration of Q on model estimates of shoreline change were performed by integrating Q from the coast to 8, 10, and 15 m isobaths. The closure depths were kept constant in the alongshore. About 80% of the alongshore sediment transport was estimated to occur between 0–

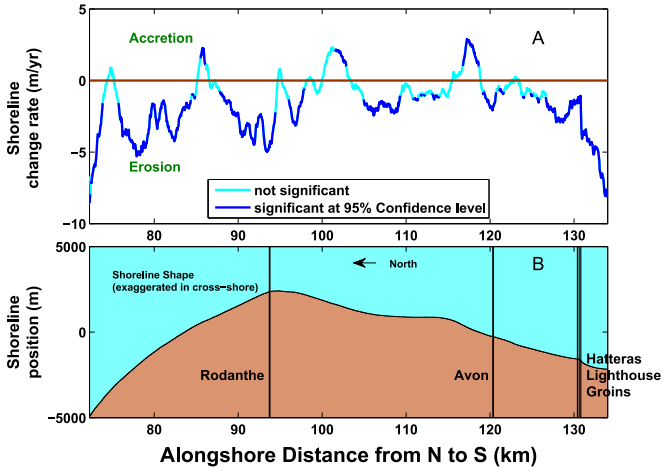

Fig. 2. (A) Alongshore variation of rate of shoreline change estimated based on 14 aerial photographs of the coast taken between 1979–2002. Y-axis of panel (B) is exaggerated in the cross-shore direction in order to better see the relative promontories and embayments in the shoreline. (For interpretation of the references to color in this figure legend, the reader is referred to the web version of this article.)

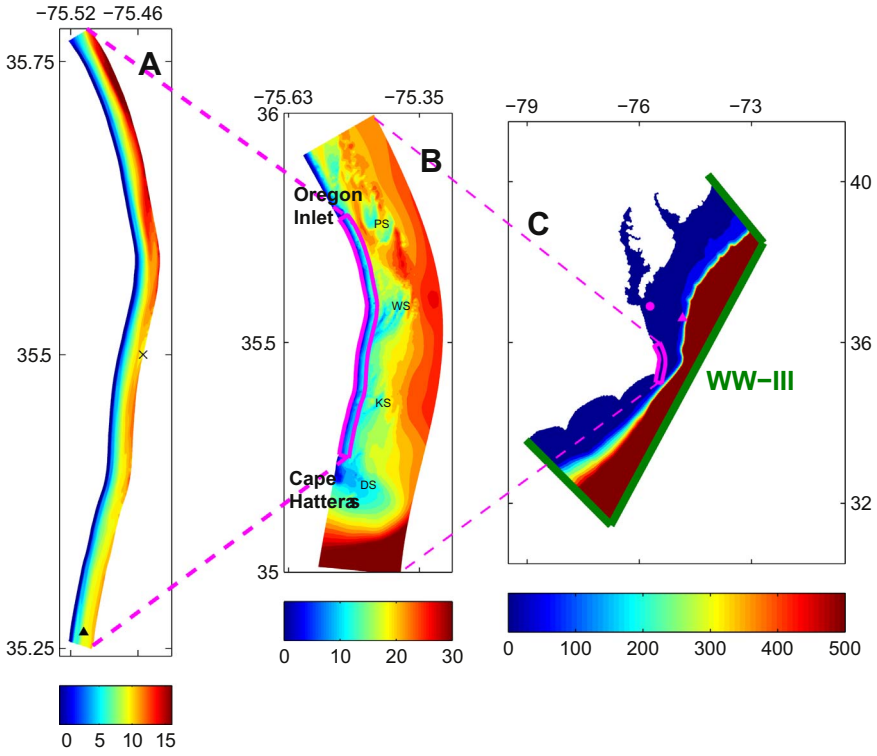

Fig. 3. Triple-nested grid setup and bathymetries: (A) nearshore grid (5–40 m resolution); (B) shelf grid (400-m resolution); (C) offshore grid (2-km resolution). The black triangle in panel (A) denotes the location of wave height measurements in the 2010 experiment; the 'x' in panel (A) denotes the center of the offshore boundary of the nearshore grid where the wave conditions in Fig. 10 correspond to; the magenta triangle and circle in panel (C) denote the location of the NDBC buoys 44014 and CHLV2, respectively. The shoal features of Platt Shoals (PS), Wimble Shoals (WS), Kinnakeet Shoals (KS) and Diamond Shoals (DS) are labeled in panel (B). (For interpretation of the references to color in this figure legend, the reader is referred to the web version of this article.)

8 m, 12% between 8–10 m, and 8% between 10–15 m. Using the different integration depths did not change the computed alongshore patterns of shoreline change, therefore, calculations based on integrating up to 15 m were used and d is taken as 15 m in Eq. (5).

4.4. Modeling approach

4.4.1. Computational grids

Simulations were computed on a series of refined grids (Fig. 3), allowing the generation of large scale processes to drive smaller scales. The coarsest parent grid (offshore grid; Fig. 3c) spans along the US east coastline beginning north of Delaware Bay and extending to the south to Myrtle Beach. The grid has approximately a 2-km resolution (257×171 cells). The intermediate grid (shelf grid; Fig. 3b) extends from approximately 36°N to 35°N latitude of the North Carolina coast to about 15-km offshore with 400-m resolution (41×259 cells). The shelf grid includes the inner shelf shoal features (Fig. 3b). The third and the finest grid (nearshore grid; Fig. 3a) starts from about 1-km south of the Oregon Inlet and extends to 1.2-km north of Cape Hatteras. This nearshore grid extends about 0.2-km landward of the shoreline and about 1.8 km offshore, yielding 2 km cross-shore extent. The grid resolution increases from 40-m at its offshore boundary to 5-m in the shallow areas in order to resolve the surf zone processes (100×1522 cells).

The bathymetry within the extent of the nearshore grid reflects a three-dimensional nearshore morphology that is likely to be ephemeral and changing on the cycle of storms and fair weather periods. The available data sets to create the bathymetry of the nearshore grid (LIDAR, single-beam and swath data; Section 3.2) are from 2001, 2002 and 2009 and obviously do not correspond to the actual bathymetry at the beginning of the period studied (1979), which is not available. Therefore, in order to remove ephemeral bathymetric features, the bathymetry was smoothed by moving averaging within 2-km windows in the alongshore direction. After smoothing, the bathymetry was shifted in the cross-shore direction such that the location of the shoreline elevation (1.2 m above sea level, i.e., z=−1.2 m with respect to NAVD88) on each profile matches the actual location of the mean shoreline (mean of the 14 shoreline positions available from the shoreline data; Section 3.1) on that profile. Finally, the bathymetry near the open boundaries of the nearshore grid was merged with the shelf grid to create a smooth transition between them.

4.4.2. Morphological feedback

In the adjustment of the bathymetry with respect to the shoreline, the mean shoreline was used instead of the initial (1979) and final (2002) shorelines and the shoreline on the LIDAR data set (Section 3.2). The reason is to reduce the effect of ephemeral irregularities of any single shoreline, essentially the same reason for smoothing of the available bathymetry in the first place. It would be ideal to initialize the model with the full topography and bathymetry corresponding to 1979 and also have the full topography and bathmetry corresponding to 2002 to test the model results, and run the model with morphological feedback through the 1979–2002 time period. However, such topography and bathymetry data sets are not available for our study area; and such data sets are rarely, if ever, available anywhere to our knowledge. In fact, for numerical modeling of the O(10-km) spatial scales we focus in this study, the seamless bathymetry we have between the coastline and the outer shelf is a rare advantage for modeling. In addition, full hydrodynamic and morphological feedback over a 24-yr-long time period is not possible with current modeling capabilities for any modeling system to our knowledge, in part because of the inadequacies of long-term cross-shore transport modeling, and also because of the development of model-related instabilities.

To see if morphological feedback is necessary, model bathymetries were also constructed using the smoothed initial (1979) and final (2002) shorelines. Comparison of model results based on these bath-

ymetries represents the most extreme test of whether a changing shoreline position affects the transport gradients to a degree that indicates that morphological feedback could be important in our study. Forced by the same set of wave conditions, these cases produced nearly the same alongshore sediment transport rates, and thus would generate similar alongshore gradients of transport. This indicates that the shoreline change between 1979 and 2002 would not be enough to change the shoreline shape to the degree that sediment transport and its gradients would change the morphology enough to in turn affect the feedback, and including morphological feedback in the modeling approach is not necessary in our case. The overall shape of the coast, major curvature of the shoreline (Fig. 2b) and the offshore shoal features are more influential than the changes in shoreline position between 1979 and 2002 to change the predicted sediment transport patterns over the large scales of interest here.

4.5. Model setup

Numerical simulations using SWAN to compute wave fields were performed on the triple-nested grid setup for 24 yr between 1979 and 2002. The simulations were conducted on the offshore grid using a 300-s time step and driven by data from WaveWatchIII (Section 3.3) along the open boundaries. Results of directional wave spectra were saved in this offshore grid at the boundary points of the shelf grid. Then the shelf grid was simulated (300-s time step) for the same time periods and likewise provided boundary data for the nearshore grid. For all three grids, the same wind forcing (Section 3.3) and physics options were prescribed. Depth-limited wave breaking was accounted for using the Battjes and Janssen [4] formulation with a constant ratio of maximum individual wave height over depth; bottom friction dissipation was activated using the default JONSWAP formulation [22]. Although there can be rare strong inner-shelf flows during strong wind events, we assume that during the period of this study the sediment transport patterns affecting the shoreline change estimates computed on the nearshore grid are dominated by wind and wave-induced flows in the nearshore. Therefore, only waves were modeled in the offshore and shelf grids. On the nearshore grid, SWAN and ROMS were run in a two-way coupled sense in order to resolve the wave, circulation, and sediment transport processes. Synchronous exchange of data fields between SWAN and ROMS occurred on an hourly interval. At the open boundaries of the nearshore grid, zero-gradient boundary condition was used for the free-surface, depth-averaged and baroclinic velocity fields. The model domain was resolved to have 10 vertical levels. In the simulations, the sediment parameters were kept spatially and temporally constant: fine sand with median diameter of D_{50}=250 μm ([24]; their Fig. 6). In this finest grid (computationally most expensive), simulating each year (1979–2002) with 2-s time step for ROMS and 120-s time step for SWAN takes about three weeks on 96 parallel-running processors.

4.6. Model evaluation

Numerical results were evaluated within the modeled area using available observational data. Two nearby buoys, NDBC 44014 (36.611 N 74.842 W; magenta triangle in Fig. 3c; 50 m depth) and NDBC CHLV2 (36.905 N 75.713 W; magenta diamond in Fig. 3c; 20 m depth), provided data on bulk wave parameters between 1996 and 2002. Model-data comparisons of significant wave heights at these two buoys in different years are shown in Figs. 4 and 5; r^2=0.78 for 44014 (Fig. 4) and 0.7 for CHLV2 (Fig. 5); the average root-mean-square-error (RMSE) is 35 cm for both buoys, with an average model-data regression slope of 0.9. The errors are mostly such that wave energy during energetic storms is underpredicted and wave energy during calm periods is overpredicted. These errors could partly be attributed to errors in the NARR wind hindcasts which are the only source of wind information for the modeled period. NDBC 44014 is directional, therefore, the mean wave directions observed and modeled at this buoy for the year with the most complete record (1999) are shown in Fig. 6, together with significant wave height and period; the model-data comparison is very good (r^2=0.65 for wave direction and r^2=0.61 for wave period). Model results were also evaluated with the wave data collected during a nearshore processes field experiment off Cape Hatteras for about two months between February-March 2010 to study storm-induced coastal change processes ([40]). The site that was

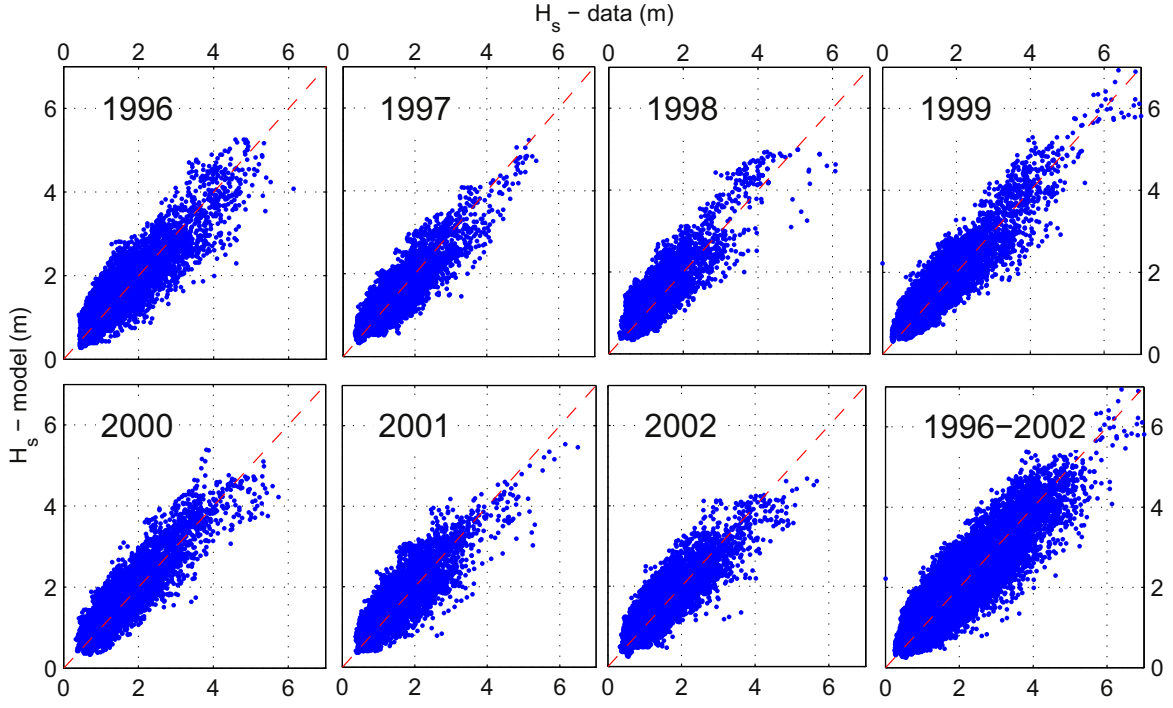

Fig. 4. Model-data comparison of significant wave height at the NDBC 44014 buoy (magenta triangle in Fig. 3c) in 1996–2002. Dashed red lines show the one-to-one relationships. (For interpretation of the references to color in this figure legend, the reader is referred to the web version of this article.)

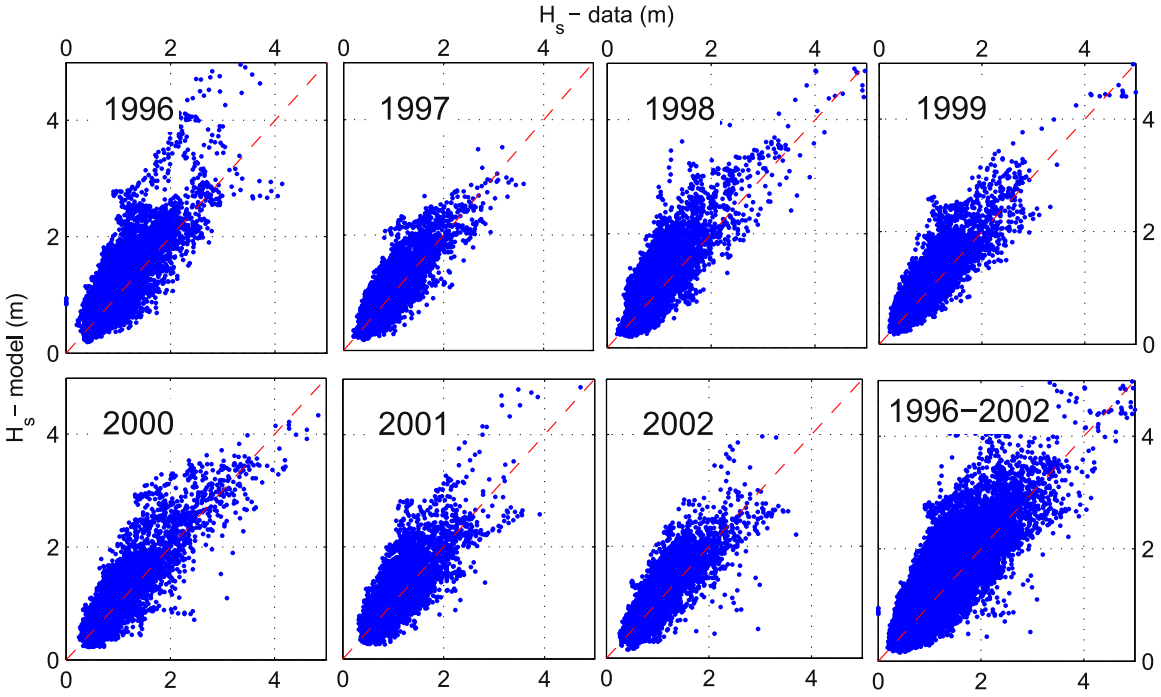

Fig. 5. Model-data comparison of significant wave height at the NDBC CHLV2 buoy (magenta circle in Fig. 3c) in 1996–2002. Dashed red lines show the one-to-one relationships. (For interpretation of the references to color in this figure legend, the reader is referred to the web version of this article.)

deployed within the domain of our nearshore grid was located about 1-km offshore (black triangle in Fig. 3a, ~10-m deep) for the entire duration of the experiment. The same triple-nested grid setup and sources of forcing data (WaveWatchIII wave boundary conditions, NARR winds) that were used in modeling of the 1979–2002 period were also used for the simulation of this experiment. The experiment captured a few events during which wind speed exceeded 15 m/s and significant wave height exceeded 3-m (Fig. 7). Fig. 7 shows the model-data comparison with r^2=0.68 and RMSE=50 cm. The model reasonably captures the variation of observed wave energy (model-data regression slope of 0.96, i.e., slight underprediction by the model) and direction (regression slope of 0.99) in the nearshore, therefore, we proceeded to run the model for our 24-yr period of interest and analyze its results. We are aware that testing the wave prediction is not a full test of the model. However, no data set is available to test the model for nearshore sediment transport other than observations of shoreline change, mainly due to complexities of collecting relevant and reliable direct field measurements of sediment fluxes over the temporal

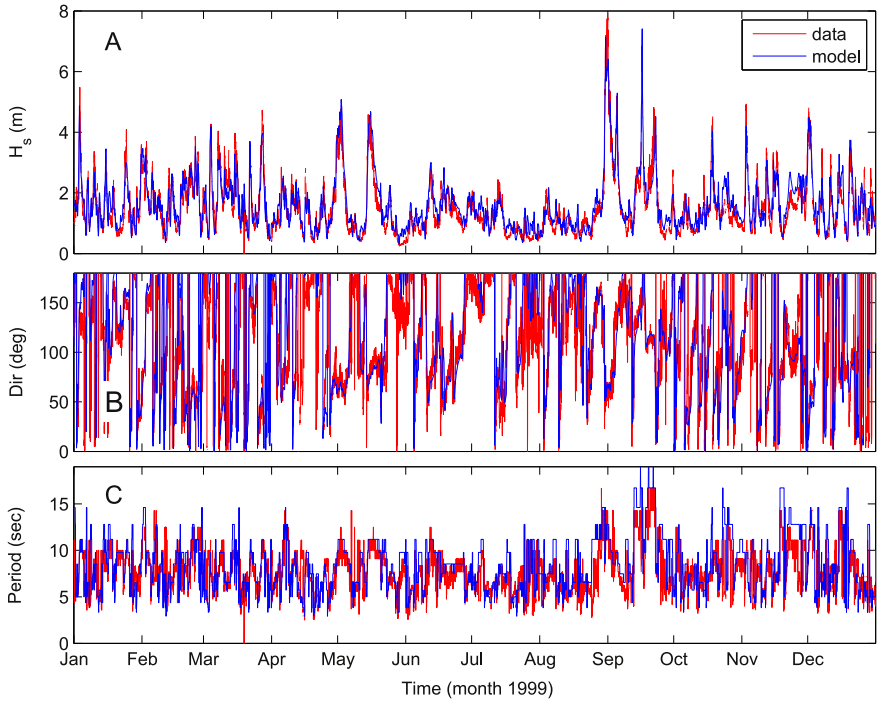

Fig. 6. Model-data comparison of (A) significant wave height, (B) mean direction (for clarity, only onshore wave directions are shown) and (C) period at the NDBC 44014 buoy (magenta triangle in Fig. 3c) in 1999. (For interpretation of the references to color in this figure legend, the reader is referred to the web version of this article.)

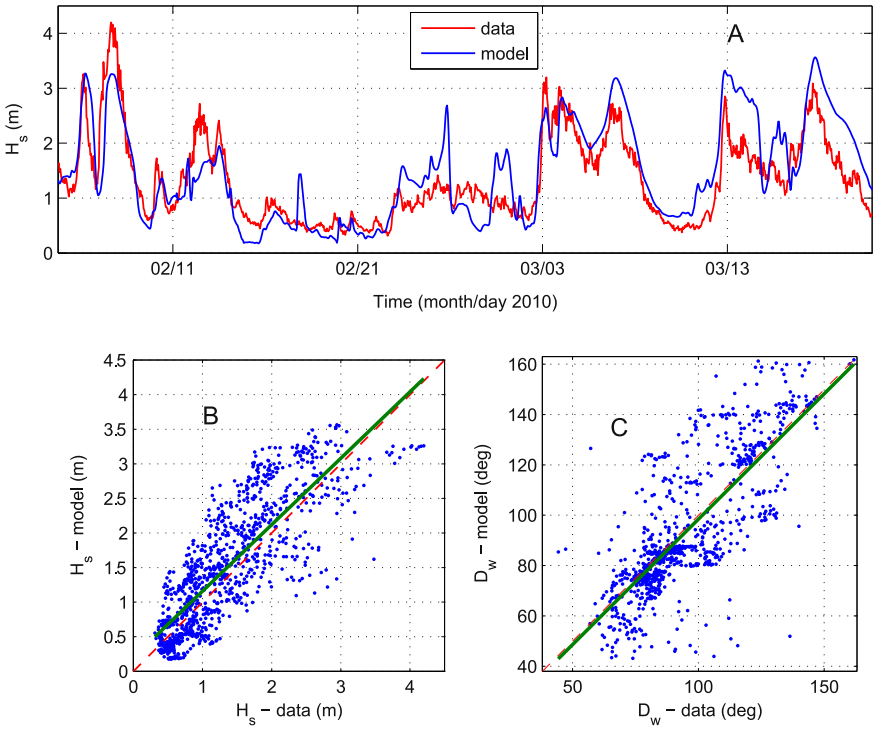

Fig. 7. Model-data comparison of significant wave height and direction in the 2010 experiment (black triangle in Fig. 3a). In panels B and C, dashed red lines show the one-to-one relationships and green lines show the best-fit based on the linear regression. (For interpretation of the references to color in this figure legend, the reader is referred to the web version of this article.)

(decadal) and spatial scales (tens of km) we focus here. The reader is referred to Kumar et al. [30] demonstrating several validations of the modeling system for nearshore flows using available data from Duck, North Carolina.

Within the Oregon Inlet-Cape Hatteras section, tidal currents are relatively small [1], with the semidiurnal M_2 being associated with the largest tidal amplitude of 47 cm and strongest tidal current of about 10 cm/s [36,8]. The effect of tides on sediment transport patterns calculated was tested by turning the tides in the simulations on and off. Tides were seen to affect the cross-shore location of maximum alongshore sediment transport: the peaks in low- and high-tide phases occur farther offshore and closer to shore, respectively, compared to the cross-shore variation of alongshore sediment transport calculated with no tide forcing. Compared to no-tide case, high-tide conditions mostly result in more transport which could be attributed to a concentrated surf zone. Low-tide conditions mostly result in less transport than no-tide case. However, differences in the cross-shore integrated alongshore sediment transport rates between the no-tide case and the tide case that would affect the results here, and changes in the alongshore gradients of alongshore transport were even smaller. Therefore, results obtained with no tidal forcing are presented in this study. Sensitivity of shoreline change estimates to sediment parameters set in the model (such as erosion rate, settling velocity, and critical stress for erosion) was also tested; no effect on alongshore trends of alongshore sediment transport or erosion and accretion patterns was seen.

4.7. Empirical transport formula

To see the effects and clarify possible advantages of using a more advanced model, the sediment transport estimates obtained with the hydrodynamics-based COAWST model are compared with one of the most frequently-used empirical formulas that is based on local breaking wave characteristics. This empirical estimate of alongshore sediment flux (Q_e) in the so-called 'CERC' approach is found as, in m^3/s [67]:

$$Q_e = \frac{K\rho\sqrt{g}}{16\sqrt{\gamma}(\rho_s - \rho)(1-n)} H_b^{2.5}\sin(2\alpha_b), \tag{6}$$

where ρ is water density, γ=0.78, n is porosity, H_b is the root-mean-square wave height at breaking, α_b is the breaking wave angle relative to shore-normal, and K is an empirical coefficient. To get CERC estimates that are of the same order of magnitude with the observation-derived and hydrodynamics-based-modeled alongshore sediment transport rates, K=0.2 is used herein. As noted in Section 1, these formulations are poorly constrained and their empirical coefficients span a few orders of magnitude in the literature. The objective here is to compare the alongshore variations of alongshore sediment transport computed using a hydrodynamics-based model and with an empirical formula, rather than to compare absolute magnitudes.

The breaking point was located by analyzing the COAWST model estimates of cross-shore evolution of wave energy dissipation due to breaking. Accordingly, using the COAWST wave computations for 1979–2002, wave breaking characteristics (height and angle) for Eq. (6) were obtained where the ratio of root-mean-square wave height to water depth reaches 0.3 [38].

5. Results

The rate of observed shoreline change is estimated using the shoreline positions and analysis method as described in Section 3.1. The hydrodynamics-based model, on the other hand, computes alongshore sediment transport fluxes (Sections 4.1 and 4.5). In order to provide a model-data comparison, the observed shoreline change rate is converted to an estimate of net alongshore sediment transport flux, and the modeled alongshore sediment transport flux is converted to an estimate of shoreline change rate, using the assumptions detailed below.

5.1. Observed shoreline change rate

Fig. 2a shows the rate of shoreline change based on the analysis described in Section 3.1. Fig. 2b shows a cross-shore exaggerated

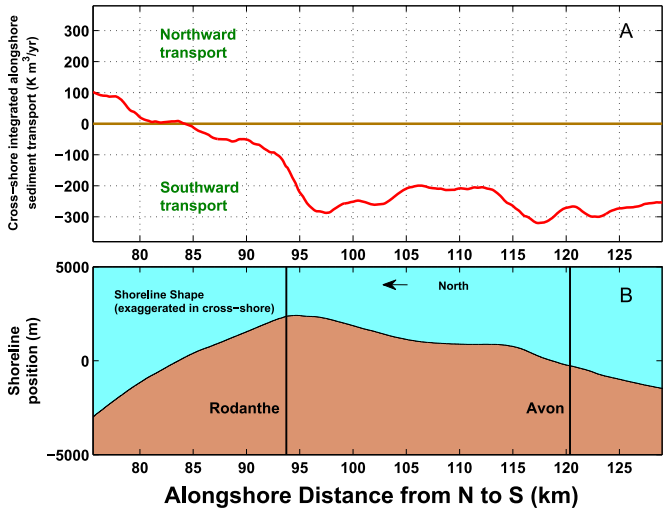

Fig. 8. (A) Alongshore variation of model-calculations of cross-shore integrated alongshore sediment transport rate (net annual). Y-axis of panel (B) is exaggerated in the cross-shore direction in order to better see the relative promontories and embayments in the shoreline. (For interpretation of the references to color in this figure legend, the reader is referred to the web version of this article.)

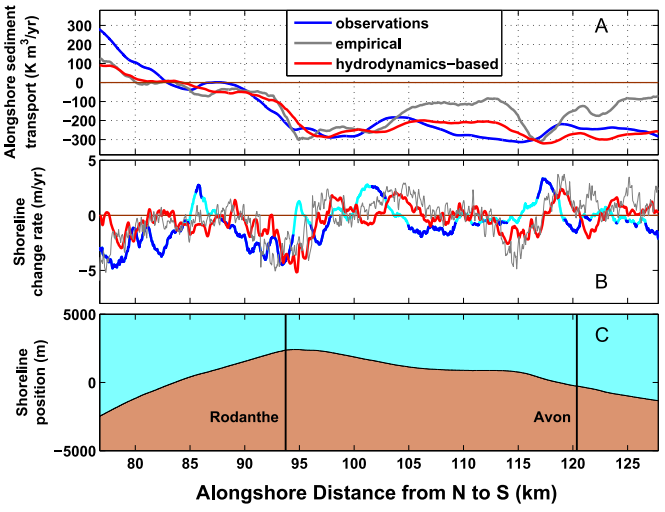

Fig. 9. Alongshore variation of (A) annual alongshore sediment transport, and (B) shoreline change rate (positive is accretion; negative is erosion). Red corresponds to the hydrodynamics-based COAWST model calculations, grey corresponds to the empirical CERC estimates, blue corresponds to the observations. Y-axis of panel (C) is exaggerated in the cross-shore direction in order to better see the relative promontories and embayments in the shoreline. (For interpretation of the references to color in this figure legend, the reader is referred to the web version of this article.)

shoreline in order to better see the relative promontories and embayments. Throughout the coverage of the 24-yr shoreline data set, the majority of the section was erosional; the average shoreline change was −1.5 m/yr, reaching to −8 m/yr around both Oregon Inlet and Cape Hatteras Point (Fig. 2a). There are a few localized accretionary zones with magnitudes of about 1–2 m/yr; two of these accretionary regions (near 102 and 117 km) are downdrift of the two relative promontories. The northern half of the section (km < 100) is associated with a higher rate of average erosion compared to the southern half.

5.2. Modeled alongshore sediment transport flux

Results from the numerical simulations were used to compute the net alongshore sediment transport flux (Q) by summing the cross-shore integrated alongshore sediment transport flux (suspended load and bedload) over the 24-yr simulation (Fig. 8a). Results show the annual net alongshore sediment transport flux varies along the coastline from 1×10^5 at the northern limit to -3.2×10^5 m^3/yr at the southern limit and that the vast majority of the study area is experiencing southward transport. There is a broad nodal point north of the major promontory near Rodanthe (Fig. 8b) between 80 and 85 km. The transport is towards the north on the north side of this nodal point, and towards the south on its south side. The nodal point of transport moves in time with the incoming wave direction that also varies in time; but this long-term average nodal point in Fig. 8b is where the time-integrated transport is zero and the shoreline is oriented 10–15° counter-clockwise from North, and located where the dominant waves from Northeast approach to perpendicular to the shoreline orientation when they reach the nearshore. The annual alongshore trends of cross-shore integrated alongshore sediment transport fluxes are similar among the different years, however, there are quantitative differences due to different forcing conditions (i.e., wave energy and directionality) in each year; for example, annual net transport near Cape Hatteras was as high as -5.5×10^5 m^3/yr southward in one year.

5.3. Model-data comparison

5.3.1. Shoreline change rate

The observed shoreline change rate is computed directly from the observations and the modeled shoreline change rate is derived quantitatively from the modeled sediment fluxes. For the observations, the data shown in Fig. 2a was adjusted to remove a component of change assumed to be due to sea level rise (result is shown in Fig. 9b), a process that is not included in our model approach. Based on the coastal orientation and exposure to waves, the section of the coast from the Rodanthe headland to a location north of the influence of Cape Hatteras and the lighthouse groins (95–125 km) is expected to have similar net alongshore sediment transport rate and direction, apart from the small variations associated with the small promontory located north of Avon (115 km). Therefore, the average shoreline change rate observed within this section, which is −0.5 m/yr, is assumed to be due to sea level rise and this constant is removed from the entire shoreline change curve. Alternatively, using a shoreface slope of 0.027 based on the bathymetry data, and a historical sea level rise rate of 0.0015 m/yr [23], the component of shoreline change due to sea level rise can be estimated using the simple Bruun Rule [10]. This gives a rate of −0.55 m/yr, almost identical to what is estimated above based on the shoreline change data.

This adjusted observed shoreline change rate and the shoreline change rate estimate based on the model calculations of alongshore sediment transport flux (Eq. (5)) are compared in Fig. 9b. The shoreline change rate estimated from the model is of the same order of magnitude as that from the observations, O(1 m/yr), and mostly erosional (60% of the section) with an average of −0.5 m/yr although the spatial patterns are fairly different in some respects and similar in others. In the northern half between 75 and 95 km, the model gives a largely erosional zone which is consistent with the same largely erosional zone shown by the observations. There is also an erosional hotspot around the major promontory near Rodanthe (between 90 and 100 km; Fig. 9b) in both the model and observations. The model captures well the observed higher rate of erosion averaged over the northern half of the section (km < 100) compared to the southern half where shoreline change is more evenly distributed between accretion and erosion. The observed shoreline change averaged over the northern half is −1.8 m/yr (erosion) and the model calculations returned −1.2 m/yr. The observed and modeled shoreline changes averaged over the southern half, on the other hand, are much smaller; −0.08 m/yr and 0.07 m/yr, respectively. There are two sections of disagreement at the relative embayments in the southern half (between 104–106 km and 124–128 km); the model estimates suggest accretion at these embayments while the observations indicate erosion. Overall, in the results from the numerical model calculations, sediment is being

laterally distributed such that the relative promontories erode (see the two major erosion peaks around 95 km and 115 km) and the relative embayments between these promontories accrete. This is consistent with previous computational findings [34,35] some of which are specifically for North Carolina Outer Banks being associated with a low-angle wave climate and diffusive shoreline [3,34].

5.3.2. Alongshore sediment transport flux

The modeled alongshore sediment transport flux was computed directly from the numerical results while an observation-derived alongshore sediment transport flux was obtained in an inverse manner from the observations of shoreline change rate. This observation-derived alongshore sediment flux is obtained based on a solution for Q in Eq. (5), with $\partial x/\partial t$ being the observed shoreline change rate and the closure depth taken as d=15 m, the same depth used as the offshore limit of the alongshore flux integration in the model results. This inverse computation of flux requires an alongshore sediment flux value known somewhere along the coast as the shoreline change rate is reflective of alongshore gradients of alongshore sediment flux, not the magnitude. It is, unfortunately, not possible to determine such a value solely from the observations of shoreline change rate. However, the major area of erosion in the observations is north of the Rodanthe headland which might imply a sediment transport divergence in the vicinity. Therefore, a nodal point where the observed alongshore sediment flux is zero is assumed to be located in this region, between 80 and 90 km. This is also reasonable geomorphically because of the changing coastline curvature in that region and the observation that sediment becomes impounded by the terminal groin on the south side of the Oregon Inlet, indicating northward transport there. Sensitivity tests showed that setting the flux to zero anywhere between 85 and 90 km makes little difference in the observation-derived alongshore sediment flux curve and we use 88-km here. It should be noted that the location of the nodal point, or setting the flux to any other value at any other location, does not affect the shape or slope of the observation-derived alongshore sediment transport curve, but merely offsets the entire curve by a constant.

Observed-shoreline-derived and modeled net alongshore sediment transport fluxes are compared in Fig. 9a. Based on the observations, the alongshore sediment transport fluxes range from 3×10^5 to -3.2×10^5 m^3/yr and are of the same order of magnitude, $O(10^5)$ m^3/yr, with those computed from the model (Section 5.2). Both in the observations and the model results north of km-95, alongshore sediment transport rapidly changes, resulting possibly from the continuously curving coastline and alongshore variations in shelf bathymetry (Fig. 3b). South of km-95 where the orientation of the coast is relatively uniform compared to the northern section, the changes in the modeled and observed transport rates are much less rapid. It should be noted that the removal of the shoreline change rate component assumed to be due to sea level rise (Section 5.3.1) affects the slope of the inverse-calculated alongshore sediment transport curve. But nevertheless, this removal results in the relatively uniform alongshore sediment transport of $\sim-3\times10^5$ m^3/yr within the 95–125 km zone, consistent with our expectation for that section (Section 5.3.1). In addition, the difference between the North and South sections, evident both in the observed and modeled transport patterns, still holds.

The CERC estimate for the modeled period (1979–2002) aligns well with the hydrodynamics-based estimate between 75 and 93 km (Fig. 9a). Both the hydrodynamics-based estimates and CERC estimates are in agreement with the observations from the northern limit to approximately km-93. At south of this point, the hydrodynamics-based model is showing differences which return a better agreement with the observations of alongshore sediment transport, especially near and between the promontories at km-95, km-115, km-121. The CERC estimate has greater alongshore variations with weaker transport from km-105 to 115 and from km-120 to 130. Shoreline change rates from CERC are relatively noisy (reasons are discussed below in Section 5.4) and show deviations from the hydrodynamics-based estimates also at south of km-93 (Fig. 9b), similar to the comparison of alongshore sediment transport patterns (Fig. 9a). The processes controlling these alongshore sediment transport patterns are investigated in details in the next section.

5.4. Transport diagnostics

To investigate the major processes influential on alongshore flows and alongshore sediment transport, two storm instances within the modeled period (in January 1993 and in January 1995; see the dashed magenta lines in Fig. 10) were selected. These times were selected because each storm was associated with strong wave action (~4-m waves at 10-m depth) but with different directionalities (from ~80°, i.e., ENE, and ~120°, i.e., ESE at 10-m depth). Fig. 11 presents the major terms of the cross-shore integrated alongshore momentum balance (Fig. 11a and d) and the cross-shore integrated alongshore sediment transport flux (Fig. 11b and e). During the January 1993 storm, waves are from ENE and the alongshore sediment transport flux (Fig. 11b) is directed southward. The momentum balance (Eq. (1)) has five main contributions from wave breaking, bottom stress, alongshore pressure gradient, horizontal advection, and vortex force terms (Fig. 11a); the other terms are negligibly small here and are not shown. The wave-breaking term (the non-conservative effect of waves on mean currents; grey curve in Fig. 11a) is directed southward in the direction of breaking waves, and is the main term driving the flow. The bottom stress is in the opposite direction and acts to reduce the flow (blue curve in Fig. 11a). The horizontal advection (black curve) and vortex force (conservative effect of waves on mean currents; magenta curve) are in opposite directions of each other. Finally, the pressure gradient (green curve) has a contributing magnitude that varies in sign, especially near the promontories. These balances show that besides wave breaking, the other terms of bottom stress, pressure gradient, horizontal vortex force and horizontal advection also contribute to the alongshore momentum balance, differing from the conventionally accepted simple alongshore balance between wave breaking and bottom stress. The alongshore balance is similar for waves from ESE (Fig. 11d–f) except that the momentum terms and the transport have opposite signs compared to the ENE-wave case (Fig. 11a–c). In this case the significance of the terms beyond wave breaking and bottom stress terms is even more clear. The similarities between the net annual cross-shore integrated alongshore sediment transport trends (Fig. 8a) and the alongshore sediment transport variation obtained especially for the first diagnosed storm (waves from ENE; Fig. 11b) suggest that the momentum balance terms discussed above are relevant for explaining the long-term alongshore transport patterns as well.

To compare the performance of the more sophisticated hydrodynamics-based model to the empirical CERC formulation, the alongshore sediment fluxes computed from both approaches are shown for each storm (Fig. 11b and e). Similar to the comparison of long-term alongshore sediment transport (Section 5.3.2, Fig. 9a), COAWST estimate of transport and the CERC formulation for the two storms are similar between 75 and 93 km (Fig. 11b and e). However, the difference between the two estimates are prominent South of km-93, near and between the promontories. In general, the empirical CERC results are inherently more noisy (variations on less than 1-km scale) as compared to COAWST because CERC is based on local quantities and all small variations in wave breaking along the coast create variations in that solution. Wave breaking term in COAWST (first term on the right hand side of Eq. (1)) and the CERC formulation (Eq. (6)) follow very similar patterns in both cases (grey curves in Fig. 11a, b, d, and e). However, the COAWST model contains other processes such as advection and vortex force that are driven by larger scale processes and tend to smooth out small scale gradients. During the storm with waves from the ENE, the COAWST and CERC results are similar from the north end to approximately km-93 where the CERC results start to show more larger scale variability. For example, near km-116, the

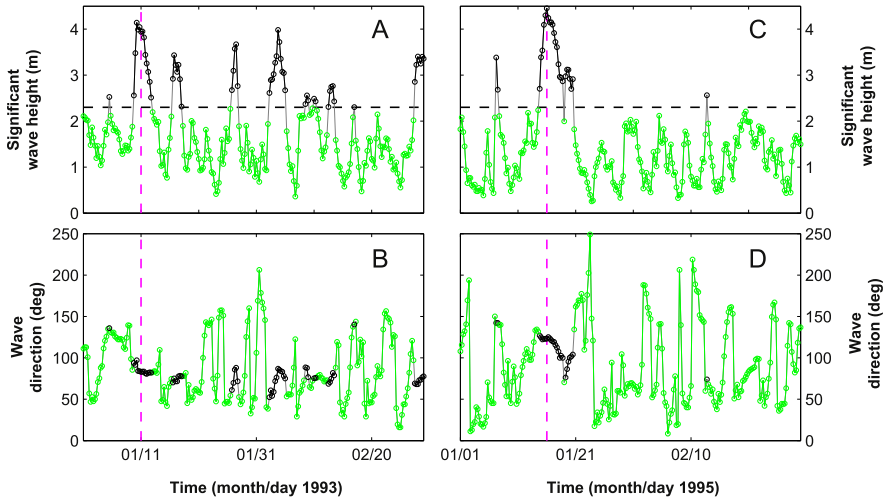

Fig. 10. Model calculations of significant wave height (panels A and C) and wave direction (panels B and D) in January-February 1993 (left) and 1995 (right), at the center of the offshore boundary of the nearshore grid ('x' on Fig. 3a). Black and green denote big- and small-wave events, respectively. Black dashed lines correspond to H_s=2.3 m, threshold of big wave events (highest 10%), and magenta dashed lines correspond to instances where the terms in the alongshore momentum balance are demonstrated in Fig. 11. Wave directions indicate where waves are coming from and are measured clockwise with respect to North, e.g., 90° indicates waves from the East. (For interpretation of the references to color in this figure legend, the reader is referred to the web version of this article.)

CERC results (Fig. 11b) have an alongshore slope that is strongly coherent with the wave breaking term from COAWST (Fig. 11a). The sudden increase in alongshore sediment flux in CERC is due to the sudden increase in the alongshore component of wave breaking. In COAWST, this process also occurs, however, the other processes such as horizontal advection will redistribute some of that momentum along the coast. Also, the pressure gradient term changes sign due to an increase in water level at this location due to increased wave breaking, which tends to reduce the transport on the upstream side of the increased wave breaking zone. In comparison for the storm with waves from ESE (Fig. 11e), similar effects can be observed such as larger CERC variations and similar response of CERC to wave breaking. In summary, although the empirical CERC formulation shows similar alongshore variations as the breaking term in the hydrodynamics-based model, the vortex force, horizontal advection and pressure gradient terms added by the model evidently modify the sediment transport estimates. The better agreement of the hydrodynamics-based model results of sediment transport with the observations compared to CERC estimates versus the observations, especially near and between the promontories (Fig. 9a), highlights that including the effects of these processes could improve the understanding of large-scale long-term sediment transport patterns.

6. Discussion

Comparison of the hydrodynamics-based model predictions to the empirical CERC formulation allows for a more comprehensive determination of the processes that occurred in time and spatially, as well as providing for an improved agreement in comparison to the observational data results. Comparing the results here with those based on representative forcings, i.e., input reduction, rather than full time series, and from other hydrodynamics-based approaches such as 2-D models is beyond the scope of this study but could be suggested as future work. It also needs to be noted that the analysis here showed

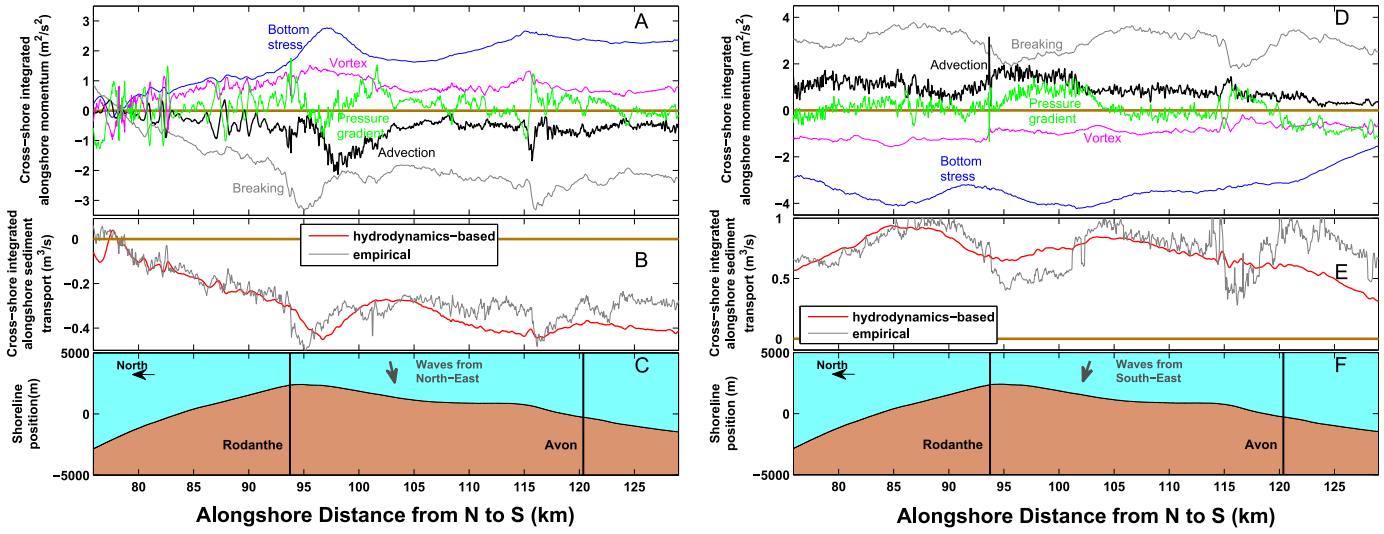

Fig. 11. Alongshore variation of model calculations of (A and D) cross-shore integrated terms in the alongshore momentum balance, and (B and E) cross-shore integrated alongshore sediment transport rate in 11 Jan 1993 (left) and 16 Jan 1995 (right). In panels (A) and (D), color coding of the terms in the alongshore momentum balance is: wave breaking (grey), bottom stress (blue), pressure gradient (green), horizontal advection (black) and vortex force (magenta). In panels (B) and (E), red and grey denote the hydrodynamics-based COAWST and the empirical CERC estimates of transport, respectively. Y-axes of panels (C) and (F) are exaggerated in the cross-shore direction in order to better see the relative promontories and embayments in the shoreline. (For interpretation of the references to color in this figure legend, the reader is referred to the web version of this article.)

that a horizontal resolution of 5 m is necessary to resolve the surf zone processes.

The model-data comparison, however, also identified several discrepancies which could be due to bathymetric uncertainties, having to use a recent bathymetry data set because of the unavailability of data during the period of interest, and processes not included in the model. The model-data discrepancy at the embayments in the south (model suggests accretion, observations indicate erosion; Fig. 9b) could be due to a possible sediment loss in these areas to the offshore. Another possible source of model error is variations in the underlying geologic framework, sediment grain size, density, and erodibility. Accounting for this geologic framework could bring additional uncertainties such as grain size variations and sediment availability. Therefore, as mentioned before, we assumed here uniform sediment parameters and did not account for the variations in geologic framework. Based on recent mapping of North Carolina inner continental shelf, Thieler et al. [63] identified portions of the inner shelf with relatively high sediment abundance (having shoreface-attached ridges and major shoal complexes) and areas where sediment is lacking (having bedforms), and showed sediment availability in the inner shelf and geometry and lithology of the shelf determine the morphology. The major shoal features in the inner shelf just offshore of our study region–Platt, Wimble, Kinnakeet, and Diamond Shoals– are evident from the bathymetry (Fig. 3b). These shoal features have an abundance of the relatively erodible and unconsolidated Holocene sand at the seafloor (see the Holocene sand thickness map in Fig. 8 in [63]). The fluvial valleys between these shoals (see Fig. 6 in [63]), on the other hand, are muddier and have less relatively erodible and unconsolidated sand (see the alongshore section in Fig. 4b in [63]). Their findings suggest that there is spatial variation in sediment parameters, sediment availability, and the overall geologic framework which we do not account for in our model calculations but are likely influential on the evolution of our shoreline section.

There is also some computational evidence for the influence of the underlying geologic framework (heterogeneities in sediments, varying thickness of sand) on the evolution of shoreline change [43] in addition to wave-driven alongshore transport and its gradients. Additionally, based on initial investigations of the effects of geologic framework in shoreline evolution ([68] using the model presented by [2]), a steady-state shoreline curvature and large scale shoreline features just north of our section were hypothesized to persist due to heterogeneous shoreface lithology and geologic framework, in spite of a low-angle wave climate and expected diffusion of the shoreline features [35]. Therefore, a more complete understanding of processes that control shoreline change may require accounting for geologic framework and processes which we do not account for in our model.

Taking into consideration the fundamental agreement of the model results with changes computed from the observations, the model results can be used to further investigate the coastal sediment transport processes. In terms of seasonality, the majority of the calculated alongshore sediment transport occurs in fall (about 50% of total), followed by winter, then spring and summer (Fig. 12), which was determined by integrating in time within the periods of four seasons. This is consistent with the higher storminess in the area during fall and winter. To investigate the temporal variability of the transport rates, the calculated net alongshore sediment transport and corresponding shoreline change are decomposed into time periods based also on the magnitude of wave events. For this decomposition, wave heights at the center of the offshore boundary of the nearshore grid ('x' on Fig. 3a) were used to determine times of relatively big-wave events versus small-wave events. Events with the highest 10% (over the period 1979–2002) of significant wave height were marked as big-wave events (H_s > 2.3–m; see the black circles and dashed black lines in Fig. 10a and c). During these big-wave events, the waves were typically dominated by approach angles from the NE-ENE sector. The rest 90% of the events ($H_s \leq$ 2.3–m; denoted by green circles in Fig. 10) over the 24 yr were marked as small-

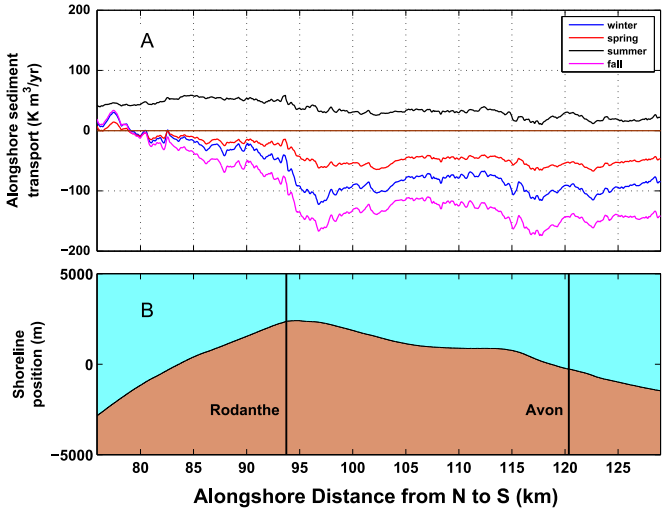

Fig. 12. Alongshore variation of seasonal alongshore sediment transport rates. Blue, red, black and purple curves correspond to integrations over winter, spring, summer, and fall seasons, respectively. Y-axis of panel (B) is exaggerated in the cross-shore direction in order to better see the relative promontories and embayments in the shoreline. (For interpretation of the references to color in this figure legend, the reader is referred to the web version of this article.)

wave events. During these small-wave events, waves were relatively uniformly distributed in terms of approach angles. During the big-wave events, the total net alongshore transport is mostly southward (black curve in Fig. 13a). The net transport from all of the smaller wave event time periods has a smaller magnitude (green curve in Fig. 13a). However, in terms of shoreline change, big- and small-wave events are associated with similar trends and similar order of magnitude of shoreline change (Fig. 13b), as the transport gradients associated with small-wave events are similar in magnitude as those associated with big-wave events. Big-wave events dominate the shoreline change in 80% of the parts where the overall model results suggest erosion, while the contribution of small-wave events is greater than big-wave events only at 20% of the erosional parts. Small-wave events make a higher contribution, compared to big-wave events, to the shoreline change in most of the accreting parts. The contribution from small-wave events is greater than from big-wave events at 67% of shoreline areas predicted as accre-

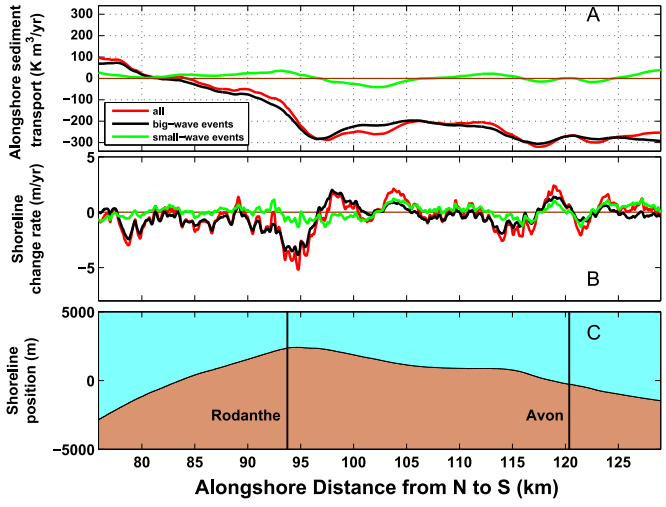

Fig. 13. Alongshore variation of model calculations of (A) annual alongshore sediment transport and (B) shoreline change rate. Green, black and red curves correspond to integrations of small wave events, big wave events, and all the events, respectively. Y-axis of panel (C) is exaggerated in the cross-shore direction in order to better see the relative promontories and embayments in the shoreline. (For interpretation of the references to color in this figure legend, the reader is referred to the web version of this article.)

tionary. These findings indicate that a small magnitude in the transport rate can be associated with large changes in shoreline change, and the actual magnitude of the transport may not be as important as the alongshore gradient of the transport.

7. Conclusion

The rate of shoreline change was investigated along an uninterrupted stretch of coastline from Oregon Inlet to Cape Hatteras of North Carolina Outer Banks for 1979–2002. We first analyzed shoreline positions obtained from aerial photographs. Results identified that most of this section eroded; the overall observed shoreline change, including the effect of sea level rise which was removed later, was −1.5 m/yr and greater in the northern half compared to the southern half. Secondly, a deterministic numerical simulation of the 24-yr period was performed using a coupled three-dimensional hydrodynamics-based model (simulated using a morphostatic sense) that accounts for wave-current interaction and sediment processes. Triple-nested grid modeling setup was forced with winds and also with validated wave hindcasts of a global wave model at its boundaries in order to include the effect of swells and distant storms, instead of a local sense which would consider only locally-generated wind waves. Despite being still computationally expensive, completion of the simulations in this first attempt shows the plausibility of using 3-D hydrodynamics-based models to investigate long-term (decadal-scale) sediment transport patterns over spatial scales of tens of km and investigating relative impacts of events of varying energy. Such hydrodynamics-based modeling allowed to rely less on reduced physics, resolve more processes, and reveal more insight to their dynamics. Thirdly, an empirical formulation was used to compute alongshore sediment transport fluxes using wave computations of the hydrodynamics-based model. These empirical results were used to assess the significance of a more simplistic approach versus an extensive hydrodynamics-based approach.

Hydrodynamics-based calculations of net alongshore sediment transport patterns indicated transport with annual rates of O(10^5 m^3/yr) southward in the vast majority of the section. Estimates from the hydrodynamic model returned shoreline change rates that are of the same order of magnitude with the observed rates of change, O(1 m/yr) and an average of −0.5 m/yr. In addition, the model results indicate a much greater erosion rate averaged over the northern half (~−1 m/yr erosion) compared to the southern half, which is also consistent with the observations. The model tends to erode promontories and accrete embayments, a behavior which is expected considering the low-angle wave climate of the area. Although the spatial patterns of observed and modeled shoreline change are different in some parts of our section, the comparison between the model calculations of net alongshore sediment transport rate and the one inversely estimated from the observed shoreline change (also O(10^5 m^3/yr)) is promising. The model also captures the observed alongshore sediment transport pattern difference between the north (where coastline curves continuously and transport changes are rapid) and south of the section (with relatively uniform orientation where transport changes are less rapid). Alongshore flow and sediment transport were shown to be governed by a balance including strong contributions from the pressure gradient, horizontal advection and horizontal vortex force, in addition to wave breaking and bottom stress. Although an empirical estimate of alongshore sediment flux reasonably matches the alongshore variations in the breaking term of the hydrodynamics-based model, accounting for these other essential processes in the model causes evident differences in the results and returns a better agreement with the observed alongshore sediment transport. Another key finding is that net alongshore sediment transport is strongly dominated by events associated with high wave energy; however, both big- and small- wave events cause shoreline changes of the same order of magnitude due to similar magnitude gradients in the alongshore transport in spite of different magnitude transport.

The differences between the observations and the estimates based on the model calculations could be attributed, in part, to uncertainties related to the observations, bathymetry, and to processes not included in the model (e.g., challenges of modeling the wave-induced effects on cross-shore sediment transport). Observational and modeling studies over the last decade, including near our study site, indicate the underlying geologic framework, such as varying sediment type and availability, may also contribute to alongshore sediment transport patterns in the nearshore and coastal change, in addition to wave-induced alongshore flows.

Acknowledgements

The first author was supported by a United States Geological Survey Mendenhall Research Fellowship. This study was also supported by the United States Geological Survey Coastal Change Processes Project and Department of the Interior Hurricane Sandy Recovery program.

References

[1] B.N. Armstrong, J.C. Warner, G. Voulgaris, J.H. List, E.R. Thieler, M.A. Martini, E. Montgomery, J. McNinch, J.W. Book, K. Haas, Carolinas Coastal Change Processes Project Data Report for Nearshore Observations at Cape Hatteras, North Carolina, February 2010, U.S. Geological Survey Open-File Report 2012-1219, 2013. ⟨http://pubs.usgs.gov/of/2012/1219/⟩.

[2] A.D. Ashton, A.B. Murray, High-angle wave instability and emergent shoreline shapes: 1. Modeling of sand waves, flying spits, and capes, J. Geophys. Res. 111 (2006) F04011. http://dx.doi.org/10.1029/2005JF000422.

[3] A.D. Ashton, A.B. Murray, High-angle wave instability and emergent shoreline shapes: 2. Wave climate analysis and comparisons to nature, J. Geophys. Res. 111 (2006) F04012. http://dx.doi.org/10.1029/2005JF000423.

[4] J.A. Battjes, J.P.F.M. Janssen, Energy loss and setup due to breaking of random waves, in: Proceedings of the ASCE International Conference on Coastal Engineering, 1978, pp. 569–587.

[5] A. Bayram, M. Larson, H. Hanson, A new formula for the total longshore sediment transport rate, Coast. Eng. 54 (2007) 700–710.

[6] C.J. Bender, R.G. Dean, Wave field modification by bathymetric anomalies and resulting shoreline changes: a review with recent results, Coast. Eng. 49 (2003) 125–153.

[7] L. Benedet, J.H. List, Evaluation of the physical process controlling beach changes adjacent to nearshore dredge pits, Coast. Eng. 55 (2008) 1224–1236.

[8] B.O. Blanton, F.E. Werner, H.E. Seim, R.A. Luettich Jr., D.R. Lynch, K.W. Smith, G. Voulgaris, F.M. Bingham, F. Way, Barotropic tides in the South Atlantic Bight, J. Geophys. Res. 109 (2004) C12024. http://dx.doi.org/10.1029/2004JC002455.

[9] N. Booij, R.C. Ris, L.H. Holthuijsen, A third-generation wave model for coastal regions, part I: model description and validation, J. Geophys. Res. 104 (C4) (1999) 7649–7666.

[10] P. Bruun, Sea level rise as a cause of shore erosion, J. Waterw. Harb. Div. ASCE 88 (1) (1962) 117–130.

[11] A. Chawla, D.M. Spindler, H.L. Tolman, Validation of a thirty year wave hindcast using the climate forecast system reanalysis winds, Ocean Model. 70 (2013) 189–206. http://dx.doi.org/10.1016/j.ocemod.2012.07.005.

[12] M.A. Dabees, J.W. Kamphuis, NLINE: efficient modeling of 3-D beach change. in: Proceedings of the 27th International Conference on Coastal Engineering, Sydney, Australia, ASCE, 2001, pp. 2700–2713.

[13] A.G. Davies, L.C. Van Rijn, J.S. Damgaard, J. Van de Graaff, J.S. Ribberink, Intercomparison of research and practical sand transport models, Coast. Eng. 46 (2002) 1–23.

[14] A.T. Davison, R.J. Nicholls, S.P. Leatherman, Beach nourishment as a coastal management tool: model description and validation: an annotated bibliography on developments associated with the artificial nourishment of beaches, J. Coast. Res. 8 (1992) 984–1022.

[15] J.F. Denny, W.C. Schwab, W.E. Baldwin, W.A. Barnhardt, P.T. Gayes, R.A. Morton, J.C. Warner, N.W. Driscoll, G. Voulgaris, Holocene sediment distribution on the inner continental shelf of northeastern South Carolina: implications for the regional sediment budget and long-term shoreline response, Cont. Shelf Res. 56 (2013) 56–70.

[16] R. Dolan, B.P. Hayden, C. Jones, Barrier island configuration, Science 204 (1979) 401–403.

[17] D. Eversole, C.H. Fletcher, Longshore sediment transport rates on a reef-fronted beach: field data and empirical models, Kaanapali Beach, Hawaii, J. Coast. Res. 103 (C8) (2003) 649–663.

[18] A. Falques, D. Calvete, Large-scale dynamics of sandy coastlines: diffusivity and

instability, J. Geophys. Res. 110 (2005) C03007. http://dx.doi.org/10.1029/2004JC002587.
[19] H. Hanson, GENESIS – a generalized shoreline-change numerical model, J. Coast. Res. 5 (1989) 1–27.
[20] C.J. Hapke, E.A. Himmelstoss, M. Kratzmann, J.H. List, E.R. Thieler, National Assessment of Shoreline Change: Historical Shoreline Change Along the New England and Mid-Atlantic Coasts: U.S. Geological Survey Open-File Report 2010-1118, p. 57, available at ⟨http://pubs.usgs.gov/of/2010/1118/⟩, 2010.
[21] C.J. Hapke, R.E. Henderson, Quantification of Shoreline Change Along Hatteras Island, North Carolina – Oregon Inlet to Cape Hatteras, 1978–2002, and Associated Vector Shoreline Data: U.S. Geological Survey Open-File Report 2015-1002, p. 13, http://dx.doi.org/10.3133/ofr20151002, 2015.
[22] K. Hasselmann, T.P. Barnett, E. Bouws, H. Carlson, D.E. Cartwright, K. Enke, J.A. Ewing, H. Gienapp, D.E. Hasselmann, P. Kruseman, A. Meerburg, P. Muller, D.J. Olbers, K. Richter, W. Sell, H. Walden, Measurements of wind-wave growth and swell decay during the Joint North Sea Wave Project (JONSWAP), Dtsch. Hydrogr. Z. Suppl. 12, A8, 1973.
[23] B.P. Horton, W.R. Peltier, S.J. Culver, R. Drummond, S.E. Engelhart, A.C. Kemp, D. Mallinson, E.R. Thieler, S.R. Riggs, D.V. Ames, K.H. Thomson, Holocene sea-level changes along the North Carolina Coastline and their implications for glacial isostatic adjustment models, Quat. Sci. Rev. 28 (2009) 1725–1736.
[24] D.L. Inman, R. Dolan, The Outer Banks of North Carolina: budget of sediment and inlet dynamics along a migrating barrier system, J. Coast. Res. 5 (1989) 193–237.
[25] K. Kaergaard, J. Fredsoe, A numerical shoreline model for shorelines with large curvature, Coast. Eng. 74 (2013) 19–32.
[26] J.W. Kamphuis, Alongshore sediment transport rate, J. Waterw. Port Coast. Ocean Eng. 117 (6) (1991) 624–641.
[27] A.B. Kennedy, K.C. Slatton, M. Starek, K. Kampa, H.-C. Cho, Hurricane response of nearshore borrow pits from airborne bathymetric lidar, J. Waterw. Port Coast. Ocean Eng. 136 (2010) 46–58.
[28] H.J. Knebel, R.R. Rendigs, J.H. List, R.P. Signell, Seafloor environments in Cape Cod Bay, a large coastal embayment, Mar. Geol. 133 (1996) 11–33.
[29] P.D. Komar, D.L. Inman, Longshore sand transport on beaches, J. Geophys. Res. 75 (1970) 5514–5527.
[30] N. Kumar, G. Voulgaris, J.C. Warner, M. Olabarrieta, Implementation of the vortex force formalism in the coupled ocean-atmosphere-wave-sediment transport (COAWST) modeling system for inner shelf and surf zone applications, Ocean Model. 47 (2012) 65–95.
[31] N. Kumar, G. Voulgaris, J.H. List, J.C. Warner, Alongshore momentum balance analysis on a cuspate foreland, J. Geophys. Res. 118 (2013) 5280–5295. http://dx.doi.org/10.1002/jgrc.20358.
[32] Y. Kuriyama, H. Sakamoto, Cross-shore distribution of long-term average long-shore sediment transport rate on a sandy beach exposed to waves with various directionalities, Coast. Eng. 86 (2014) 27–35.
[33] J. Larson, R. Jacob, E. Ong, The model coupling toolkit: a new fortran90 toolkit for building multiphysics parallel coupled models, Int. J. High Perform. Comput. Appl. 8 (19) (2005) 277–292.
[34] E. Lazarus, A.B. Murray, Process signatures in regional patterns of shoreline change on annual to decadal time scales, Geophys. Res. Lett. 34 (2007) L19402. http://dx.doi.org/10.1029/2007GL031047.
[35] E. Lazarus, A.B. Murray, An integrated hypothesis for regional patterns of shoreline change along the Northern North Carolina Outer Banks, USA Mar. Geol. 281 (2011) 85–90.
[36] S.J. Lentz, M. Carr, T.H.C. Herbers, Barotropic tides on the North Carolina Shelf, J. Phys. Oceanogr. 31 (2001) 1843–1859.
[37] J.H. List, A.S. Farris, C. Sullivan, Reversing storm hotspots on sandy beaches: spatial and temporal characteristics, Mar. Geol. 226 (2006) 261–279.
[38] J.H. List, D.M. Hanes, P. Ruggiero, Predicting longshore gradients in longshore transport: comparing the CERC formula to Delft3D, in: Proceedings of the 30th International Conference on Coastal Engineering, San Diego, CA, World Sci., Singapore, 2006, pp. 3370–3380.
[39] J.H. List, L. Benedet, D.M. Hanes, P. Ruggiero, Understanding differences between DELFT3D and empirical predictions of alongshore sediment transport gradients. in: Proceedings of the 31st International Conference on Coastal Engineering, World Sci., Singapore, 2008, pp. 1864–1875.
[40] J.H. List, J.C. Warner, E.R. Thieler, K. Haas, G. Voulgaris, J.E. McNinch, K.L. Brodie, A nearshore processes field experiment at Cape Hatteras, North Carolina, USA, in: Proceedings of the Coastal Sedimemnts, World Sci., 2011, pp. 2144–2157.
[41] O.S. Madsen, Spectral wave-current bottom boundary layer flows. in: Proceedings of the 24th International Conference on Coastal Engineering, Research Council, Kobe, Japan, 1994, pp. 384–398.
[42] J.E. McNinch, Geologic control in the nearshore: shore-oblique sandbars and shoreline erosional hotspots, Mid-Atlantic Bight, USA, Mar. Geol. 211 (2004) 121–141.
[43] J.L. Miselis, J.E. McNinch, Calculating shoreline erosion potential using nearshore stratigraphy and sediment volume: Outer Banks, North Carolina, J. Geophys. Res. 111 (2006) F02019. http://dx.doi.org/10.1029/2005JF000389.
[44] R.A. Morton, T. Miller, National Assessment of Shoreline Change: Part 2, Historical Shoreline Changes and Associated Coastal Land Loss Along the U.S. Southeast Atlantic Coast: U.S. Geological Survey Open-File Report 2005-1401, p. 35, available at ⟨http://pubs.usgs.gov/of/2005/1401/⟩, 2005.
[45] A.Y. Mukai, J.J. Westerink, R.A. Luettich Jr., D. Mark, Eastcoast 2001, A Tidal Constituent Database for Western North Atlantic, Gulf of Mexico, and Caribbean Sea, US Army Corps of Engineers ERDC/CHL TR-02-24, 2002.
[46] National Oceanic and Atmospheric Administration, National Coastal Population Report: Population Trends from 1970 to 2020, p. 22, available at ⟨http://stateofthecoast.noaa.gov/features/coastal-population-report.pdf⟩, 2013.
[47] M. Olabarrieta, J.C. Warner, N. Kumar, Wave-current interaction in Willapa Bay, J. Geophys. Res. 116 (2011) C12014. http://dx.doi.org/10.1029/2011JC007387.
[48] M.F. Overton, E.A. Smyre, Evolution of the Pea Island Breach, Outer Banks, North Carolina, Shore Beach 81 (4) (2013) 23–27.
[49] D.E. Reeve, A. Valsamidis, On the stability of a class of shoreline planform models, Coast. Eng. 91 (2014) 76–83.
[50] S.R. Riggs, W.J. Cleary, S.W. Snyder, Influence of inherited geologic framework on barrier shoreface morphology and dynamics, Mar. Geol. 126 (1995) 213–243.
[51] A.L. Rogers, T.M. Ravens, Measurement of longshore sediment transport rates in the surf zone on Galveston Island, Tex. J. Coast. Res. 24 (2008) 62–73.
[52] P. Ruggiero, J.H. List, D.M. Hanes, J. Eshleman, Probabilistic shoreline change modeling, in: Proceedings of the 30th International Conference on Coastal Engineering, San Diego, CA, World Sci., Singapore, 2006.
[53] I. Safak, J.C. Warner, J.H. List, Barrier island breach evolution: alongshore transport and bay-ocean pressure gradient interactions, J. Geophys. Res. 121 (2016). http://dx.doi.org/10.1002/2016JC012029.
[54] A.H. Sallenger Jr., K.S. Doran, P.A. Howd, Hotspot of accelerated sea-level rise on the Atlantic coast of North America, Nat. Clim. Change 2 (2012) 884–888. http://dx.doi.org/10.1038/nclimate1597.
[55] W.C. Schwab, E.R. Thieler, J.R. Allen, D.S. Foster, B.A. Swift, J.F. Denny, Influence of inner-continental shelf geologic framework on the evolution and behavior of the barrier-island system between Fire Island Inlet and Shinnecock Inlet, Long Island, New York, J. Coast. Res. 16 (2000) 408–422.
[56] W.C. Schwab, W.E. Baldwin, C.J. Hapke, E.E. Lentz, P.T. Gayes, J.F. Denny, J.H. List, J.C. Warner, Geologic evidence for onshore sediment transport from the inner continental shelf: fire Island, N. Y. J. Coast. Res. 29 (3) (2013) 526–544.
[57] A.F. Shchepetkin, H.G. McWilliams, The regional ocean modeling system: a split-explicit, free-surface, topography following coordinates ocean model, Ocean Model. 9 (2005) 347–404.
[58] J.A. Smith, Wave-current interactions in finite depth, J. Phys. Oceanogr. 36 (2006) 1403–1419.
[59] E.R. Smith, P. Wang, B.A. Ebersole, J. Zhang, Dependence of total longshore sediment transport rates on incident wave parameters and breaker type, J. Coast. Res. 25 (2009) 675–683.
[60] R.L. Soulsby, J.S. Damgaard, Bedload sediment transport in coastal waters, Coast. Eng. 52 (2005) 673–689.
[61] M.L. Stutz, O.H. Pilkey, Discussion of: "P. Wang, N.C. Kraus, R.A. Davis, Total longshore sediment transport rate in the surf zone: field measurements and empirical predictions, J. Coast. Res., 14, 1998, pp. 269–282", J. Coast. Res., 15, 1999, pp. 272–274.
[62] E.R. Thieler, D.S. Foster, D. Mallinson, E.A. Himmelstoss, J.E. McNinch, J.H. List, E. Hammar-Klose, Quaternary Geophysical Framework of the Northeastern North Carolina Coastal System: U.S. Geological Survey Open-File Report 2011-1015, 2013.
[63] E.R. Thieler, D.S. Foster, E.A. Himmelstoss, Geologic framework of the northern North Carolina, USA inner continental shelf and its influence on coastal evolution, Mar. Geol. 348 (2014) 113–130. http://dx.doi.org/10.1016/j.margeo.2013.11.011.
[64] Y. Uchiyama, J.C. McWilliams, J.M. Restrepo, Wave-current interaction in nearshore shear instability analyzed with a vortex-force formalism, J. Geophys. Res. 114 (2009) C06021. http://dx.doi.org/10.1029/2008JC005135.
[65] Y. Uchiyama, J.C. McWilliams, A.F. Shchepetkin, Wave-current interaction in an oceanic circulation model with a vortex-force formalism: application to the surf zone, Ocean Model. 34 (2010) 16–35. http://dx.doi.org/10.1016/j.ocemod.2010.04.002.
[66] L. Umlauf, H. Burchard, A generic length-scale equation for geophysical turbulence models, J. Mar. Res. 61 (2003) 235–265.
[67] U.S. Army Corps of Engineers, Coastal Engineering Manual, Coastal and Hydraulics Laboratory EM 1110-2-1100, ⟨http://www.publications.usace.army.mil/Portals/76/Publications/EngineerManuals/EM_1110-2-1100_Part-03.pdf⟩, 2002.
[68] L.M. Valvo, A.B. Murray, A. Ashton, How does underlying geology affect coastline change? An initial modeling investigation, J. Geophys. Res. 111 (2006) F02025. http://dx.doi.org/10.1029/2005JF000340.
[69] L.C. Van Rijn, D.J.R. Walstra, B. Grasmeijer, J. Sutherland, S. Pan, J.P. Sierra, The predictability of cross-shore bed evolution of sandy beaches at the time scale of storms and seasons using process-based profile models, Coast. Eng. 47 (2003) 295–327.
[70] L.C. Van Rijn, A simple general expression for longshore transport of sand, gravel and shingle, Coast. Eng. 90 (2014) 23–39.
[71] P. Wang, N.C. Kraus, R.A. Davis Jr., Total longshore sediment transport rate in the surf zone: field measurements and empirical predictions, J. Coast. Res. 14 (1998) 269–282.
[72] J.C. Warner, C.R. Sherwood, H.G. Arango, R.P. Signell, Performance of four turbulence closure methods implemented using a generic length scale method, Ocean Model. 8 (2005) 81–113.
[73] J.C. Warner, C.R. Sherwood, R.P. Signell, C.K. Harris, H.G. Arango, Development of a three-dimensional, regional, coupled wave, current, and sediment-transport model, Comput. Geosci. 34 (2008) 1284–1306.
[74] J.C. Warner, N. Perlin, E. Skyllingstad, Using the model coupling toolkit to couple

earth system models, Environ. Model. Softw. 23 (2008) 1240–1249.
[75] J.C. Warner, B. Armstrong, R. He, J.B. Zambon, Development of a coupled ocean-atmosphere-wave-sediment transport (COAWST) modeling system, Ocean Model. 35 (2010) 230–244.
[76] J.C. Warner, Z. Defne, K. Haas, H.G. Arango, A wetting and drying scheme for ROMS, Comput. Geosci. 58 (2013) 54–61.
[77] J.C. Warner, J.H. List, W.C. Schwab, G. Voulgaris, B. Armstrong, N. Marshall, Inner-shelf circulation and sediment dynamics on a series of shoreface-connected ridges offshore of Fire Island, NY, Ocean Dyn. 64 (2014) 1767–1781.
[78] W. Zhang, J. Deng, J. Harff, R. Schneider, J. Dudzinska-Nowak, A coupled modeling scheme for longshore sediment transport of wave dominated coasts – a case study from the southern Baltic Sea, Coast. Eng. 72 (2013) 39–55.